Comparing the mitochondrial signatures in ESCs and iPSCs and their neural derivations

Cecilie Katrin Kristiansen[a,b1], Anbin Chen[a,b,c,d1], Lena Elise Høyland[e], Mathias Ziegler[e], Gareth John Sullivan[f,g], Laurence A. Bindoff[a,b] and Kristina Xiao Liang[a,b]*

[a] Department of Clinical Medicine (K1), University of Bergen, Bergen, Norway.
[b] Neuro-SysMed, Center of Excellence for Clinical Research in Neurological Diseases, Haukeland University Hospital, Norway.
[c] Department of Neurosurgery, Qilu Hospital and Institute of Brain and Brain-Inspired Science, Cheeloo College of Medicine, Shandong University, Jinan, China.
[d] Shandong Key Laboratory of Brain Function Remodeling, Jinan, China.
[e] Department of Biomedicine, University of Bergen, Bergen, Norway.
[f] Department of Molecular Medicine, Institute of Basic Medical Sciences, University of Oslo, Oslo, Norway; Norwegian Center for Stem Cell Research, Oslo University Hospital and University of Oslo, Oslo, Norway.
[g] Institute of Immunology, Oslo University Hospital, Oslo, Norway; Hybrid Technology Hub - Centre of Excellence, Institute of Basic Medical Sciences, University of Oslo, Oslo, Norway; Department of Pediatric Research, Oslo University Hospital, Oslo, Norway.

[1] These first authors contributed equally.

* Corresponding author
Kristina Xiao Liang
Department of Clinical Medicine (K1),
University of Bergen,
PO Box 7804,
5020 Bergen, Norway;
Tel. +47 55 97 50 96
E-mail: Xiao.Liang@uib.no

Abstract:

Embryonic stem cells (ESCs) and induced pluripotent stem cells (iPSCs) have distinct origins: ESCs are derived from pre-implanted embryos while iPSCs are reprogrammed somatic cells. Both have their own characteristics and lineage specificity, and both are valuable tools for studying human neurological development and disease. Thus far, few studies have analyzed how differences between stem cell types influence mitochondrial function and mitochondrial DNA (mtDNA) homeostasis during differentiation into neural and glial lineages. In this study, we compared mitochondrial function and mtDNA replication in human ESCs and iPSCs at three different stages − pluripotent, neural progenitor and astrocyte. We found that while ESCs and iPSCs have a similar mitochondrial signature, neural and astrocyte derivations manifested differences. At the neural stem cell (NSCs) stage, iPSC-NSCs displayed decreased ATP production and a reduction in mitochondrial respiratory chain (MRC) complex IV expression compared to ESC-NSCs. IPSC-astrocytes showed increased mitochondrial activity including elevated ATP production, MRC complex IV expression, mtDNA copy number and mitochondrial biogenesis relative to those derived from ESCs. These findings show that while ESCs and iPSCs are similar at the pluripotent stage, differences in mitochondrial function may develop during differentiation and must be taken into account when extrapolating results from different cell types.

Keywords:

IPSCs, ESCs, NSCs, Astrocytes, Mitochondrial function, Mitochondrial biogenesis.

Abbreviation list

BSA: Bovine serum albumin

DCFDA: 2′,7′-dichlorodihydrofluorescein diacetate

DCX: Double cortin

EAAT-1: Excitatory amino acid transporter 1

ESCs: Embryonic stem cells

GFAP: Glial fibrillary acidic protein

GS: Glutamine synthetase

iPSCs: Induced pluripotent stem cells

LC3B: Microtubule-associated protein 1 light chain 3β

LC-MS: Liquid chromatography-–mass spectrometry

mito-ROS: Mitochondrial ROS

MMP: Mitochondrial membrane potential

MRC: Mitochondrial respiratory chain

mtDNA: Mitochondrial DNA

MTDR: MitoTracker Deep Red

MTG: MitoTracker Green

NSCs: Neural stem cells

PDL: Poly-D-lysine

PFA: Paraformaldehyde

PGC-1α: PPAR-γ coactivator-1 alpha

PPAR-γ: Peroxisome proliferator-activated receptor-gamma

p-SirT1: Phosphorylated sirtuin 1

p-ULK1: Phosphorylated unc-51 like autophagy activating kinase 1

qPCR: Quantitative PCR

RT: Room temperature

RT-qPCR: Quantitative reverse transcription PCR

SEM: Standard error of the mean

TFAM: Mitochondrial transcription factor A

TMRE: Tetramethylrhodamine ethyl ester

TOMM20: Translocase of outer mitochondrial membrane 20

Introduction

The manipulation of cell fates through reprogramming has altered fundamental ideas about the stability of cellular identity and stimulated major research into human disease modeling, *in vitro* tissue differentiation and cellular trans-differentiation. ESCs and iPSCs have distinct origins: ESCs come from inner cell mass of the blastocyst, while iPSCs are reprogrammed somatic cells. Due to the difficulties in performing repeated studies in humans and the limited lifespan of tissues in culture, ESC models have been a major contributor to the study of human brain development and disorders. Owing to their high proliferative capacity and their ability to differentiate into any cell type, ESCs also hold great clinical potential [1], however, ethical, and technical issues have limited their applicability. The discovery of iPSCs, made by reprogramming adult somatic cells [2], does not suffer from the same restrictions. The strength of iPSC-based studies is that somatic cells are obtained directly from patients, reprogrammed, and studied *in vitro*. These models provide a unique opportunity for studying aspects of disease mechanisms in patient-specific cells and tissues, particularly in brain cells such as NSCs, neurons and glial astrocytes.

Theoretically, since both iPSCs and ESCs are pluripotent, disease models made from these should be equivalent. While some studies report that the two cell types are functionally similar [3, 4], emerging evidence suggests genetic and epigenetic differences do exist [5-9], probably reflecting technical limitations inherent in reprogramming. These findings have raised concerns about whether iPSCs are bona fide surrogates for ESCs, especially their capacity to recapitulate faithfully developmental milestones and the potential of their differentiated progeny to replace damaged or diseased cells after transplantation. Molecular and functional comparison of ESCs and iPSCs after *in vitro* differentiation is, therefore, crucial to address these concerns.

In this study, we compared mitochondrial changes occurring in human ESCs and iPSCs during the *in vitro* directed differentiation to NSCs and glial astrocytes. While ESCs and iPSCs displayed a similar mitochondrial signature, NSCs and astrocytes showed differences in multiple aspects of mitochondrial activity. Taken together, this study provides a key foundation for the further use of iPSCs in modeling human brain development and in studying neural disorders. In particular, the data suggest that it is crucial to determine whether the identified mitochondrial differences between ESC- and iPSC-derived cells might affect research applications and therapeutic potential.

Materials and Methods

Cell culture of pluripotent cells

The Norwegian Research Ethics Committee (2012/919) granted ethical approval for the project. Tissues were acquired with written informed consent from all patients. All experiments conformed to the principles set out in the WMA Declaration of Helsinki and the Department of Health and Human Services Belmont Report. Two separate fibroblast lines were used in this study: Detroit 551 (ATCC® CCL 110™, human fetal fibroblasts, female) and AG05836 (RRID: CVCL2B58, 44 years-old female fibroblasts). All fibroblasts were grown in DMEM/F12, GlutaMAX™ (Thermo Scientific, cat. no. 35050061) with 10% (v/v) FBS. Detroit fibroblasts were reprogrammed using retroviral vectors encoding POU5F1, SOX2, Klf4, and c Myc as previously described [10].

AG05836 control fibroblasts were reprogrammed by Sendai viral vectors. We employed three human embryonic stem cell lines (hESCs): the hESC line 360 (male) and line 429 (female) was obtained from the Karolinska Institute, Sweden and H1 (male) from WiCell Research Institute [1].

Both iPSC and hESC lines were maintained under feeder free conditions using Geltrex (Invitrogen, cat. no. A1413302) in Essential 8™ medium (Invitrogen, cat. no. A1517001) in 6-well plates (Thermo Scientific, cat. no. 140675). All cells were monitored for mycoplasma contamination regularly using MycoAlert™ mycoplasma detection kit (Lonza, cat. no. LT07-218).

NSC generation via neural induction and astrocyte differentiation

Neural induction was performed as previously described [11]. NSCs were maintained in StemPro NSC medium (Table S1) and seeded on Geltrex coated 6-well plates as monolayer NSCs. All NSCs used for further analysis were limited to passages 4-9.

To generate astrocytes, we used the protocol described in our previous studies [12]. Briefly, NSCs were converted into stellate-like astrocytes by culturing in differentiation medium (Table S1) for 4 weeks. Subsequent maturation in maturation medium (Table S1) was performed over one month and up to 3 months. For astrocyte differentiation, NSCs were plated on poly-D-lysine (PDL) coated coverslips (Neuvitro, cat. no. GG-12-15-PDL) and cultured in astrocyte differentiation medium (Table S1): DMEM/F-12, GlutaMAX™ supplemented with 1X N2 (Invitrogen, cat. no. 17502-048), 1X B27 (Invitrogen, cat. no. 17504044-10 ml), 200 ng/ml insulin-like growth factor-I (Sigma-Aldrich, cat. no. I3769-50UG), 10 ng/ml heregulin 1β (Sigma-Aldrich cat. no. SRP3055-50UG), 10 ng/ml activin A (Peprotech, cat. no. 120-14E), 8 ng/ml FGF2 (Peprotech, cat. no. 100-18B) and 1% FBS. The medium was changed every other day for the first week, every two days for the second week and every three days for the third and fourth week. Further, the cells were matured in AGM Astrocyte Growth Medium BulletKit™ (Lonza, cat. no. CC-3186).

Gene expression

Total RNA was isolated by the MagMAX™ 96 Total RNA Isolation Kit (Thermo Fisher Scientific, cat. no. AM1830) using the High-throughput MagMAX™ Express 96 (Thermo Fisher Scientific). The cDNA synthesis and one-step PCR were carried out using the EXPRESS One-Step Superscript™ RT-qPCR Kit (Thermo Fisher Scientific, cat. no. 11781 200). The RT-qPCR was performed using Applied Biosystems 7500 Fast Real-Time PCR Machine (Thermo Fisher Scientific). TaqMan primers for target genes were purchased from Thermo Fisher Scientific: *POU5F1* (Hs00999634_gH), *NANOG* (Hs04260366_g1) and *LIN28A* (Hs00702808_s1). The mean CT values of three technical replicates were normalized to the endogenous control gene β-Actin (Hs01060665_g1). Expression of iPSC markers was assessed by fold change by normalizing gene levels from ESC1 using the comparative ΔΔCt method.

Calcium level

Cells were incubated with 8 µM Rhod-2-AM cell permeant (Invitrogen, cat. no. R1244) for 45 min at 37°C. Subsequent flow cytometric analysis was conducted using a FACS BD Accuri™ C6 flow cytometer (BD Biosciences, San Jose, CA, USA). Data analysis was performed using Accuri™ C6 software. For each sample, over 10.000 events were

analyzed, and cell doublets excluded by gating (see Fig. S2 for gating strategy).

Mitochondrial volume and membrane potential

To measure mitochondrial volume and membrane potential (MMP), cells were co-stained with 150 nM MitoTracker Green (MTG) (Invitrogen, cat. no. M7514) and 100 nM Tetramethylrhodamine ethyl ester (TMRE) (Abcam, cat. no. ab113852) for 45 min at 37°C. Cells treated with 100 µM FCCP (Abcam, cat. no. ab120081) was used as negative control. The samples were analyzed on a FACS BD Accuri™ C6 flow cytometer and data analysis performed using the Accuri™ C6 software. Over 10.000 events per sample were analyzed and cell doublets excluded by gating.

Immunocytochemistry and immunofluorescence (ICC/IF)

Cells were fixed with 4% (v/v) paraformaldehyde (PFA) and blocked using blocking buffer containing 1X PBS, 10% (v/v) normal goat serum (Sigma-Aldrich, cat. no. G9023) with 0.3% (v/v) Triton™ X-100 (Sigma-Aldrich, cat. no. X100-100ML). The cells were then incubated with primary antibody solution overnight at 4°C and further stained with secondary antibody solution (1:800 in blocking buffer) for 1 h at room temperature (RT). IPSCs were stained for pluripotency markers using the primary antibodies rabbit anti-SOX2 (Abcam, cat. no. ab97959, 1:100), rabbit anti-Oct4 (Abcam, cat. no. ab19857, 1:100) and mouse anti-SSEA4 [MC813] (Abcam, cat. no. ab16287, 1:200). NSCs were stained with rabbit anti-PAX6 (Abcam, cat. no. ab5790, 1:100) and mouse anti-Nestin (10c2) (Santa Cruz Biotechnology, cat. no. sc23927, 1:50). Astrocytes were stained with chicken anti-GFAP (Abcam cat. no. ab4674, 1:400) and rabbit anti-DCX (Thermo Fisher Scientific, cat. no. PA5-17428, 1:100). The secondary antibodies used were Alexa Flour® goat anti-rabbit 488 (Thermo Fisher Scientific, cat. no. A11008, 1:800), Alexa Flour® goat anti-mouse 594 (Thermo Fisher Scientific, cat. no. A11005, 1:800) and Alexa Flour® goat anti-chicken 594 (Thermo Fisher Scientific, cat. no. A11042, 1:800). After incubation with secondary antibodies, the coverslips were mounted onto cover slides using Prolong Diamond Antifade Mountant with DAPI (Invitrogen, cat. no. P36962).

For staining of neurospheres, the cells were blocked with blocking buffer for 2 hrs at RT and incubated with anti-Nestin and anti-PAX6 primary antibodies (described above) overnight at 4°C. After washing the samples for 3 hrs in PBS with a few changes of buffer, incubation with secondary antibodies (as described above) was conducted overnight at 4°C in a humid and dark chamber. Coverslips were mounted using Fluoromount G (Southern Biotech, cat. no. 0100 01) before imaging was performed using the Leica TCS SP8 confocal microscope (Leica Microsystems, Germany).

ROS production

Intracellular ROS production was measured by flow cytometry using dual staining of 30 µM 2′,7′-dichlorodihydrofluorescein diacetate (DCFDA) (Abcam, cat. no. b11385) and 150 nM MitoTracker Deep Red (MTDR) (Invitrogen, cat. no. M22426), which enabled us to assess ROS level related to mitochondrial volume. Mitochondrial ROS (mito-ROS) production was quantified using co-staining of 10 µM MitoSOX™ Red mitochondrial superoxide indicator (Invitrogen, cat. no. M36008) and 150 nM MTG to evaluate mito-ROS level in relation to mitochondrial volume. The cells were

immediately analyzed on a FACS BD Accuri™ C6 flow cytometer. For each sample, more than 10,000 events were recorded, and doublets or dead cells excluded before data analysis was performed using the Accuri™ C6 software.

ATP generation assay

ATP measurements were conducted using the Luminescent ATP Detection Assay Kit (Abcam, cat. no. ab113849) according to manufacturer's protocol. Luminescence intensity was monitored using the Victor® X Light Multimode Plate Reader (PerkinElmer). Cells cultured on the same plates were incubated with Janus Green cell normalization stain (Abcam, cat. no. ab111622) and the results used to normalize ATP values to cell number.

NAD^+ metabolism and ATP measurements by liquid chromatography-mass spectrometry (LC-MS)

For NAD^+ measurements, cells were washed with PBS and extracted by addition of ice-cold 80% methanol followed by incubation at 4°C for 20 min. Cells used for ATP measurements were washed with PBS and detached by scraping. Thereafter, all samples were stored at -80°C overnight. The following day, samples were thawed on a rotating wheel at 4°C and subsequently centrifuged at 16 000 g and 4°C for 20 min. The supernatant was added to 1 volume of acetonitrile and the samples were stored at -80°C until analysis. The pellet was dried and subsequently reconstituted in a lysis buffer (20 mM Tris-HCl (pH 7.4), 150 mM NaCl, 2% SDS, 1 mM EDTA) to allow for protein determination (BCA assay).

Separation of the metabolites was achieved with a ZIC-pHILC column (150 x 4.6 mm, 5 µm: Merck) in combination with the Dionex UltiMate 3000 (Thermo Scientific) liquid chromatography system. The column was kept at 30°C. The mobile phase consisted of 10 mM ammonium acetate pH 6.8 (Buffer A) and acetonitrile (Buffer B). The flow rate was kept at 400 µl/min and the gradient was set as follows: 0 min 20% Buffer B, 15 min to 20 min 60% Buffer B, 35 min 20% Buffer B. Ionization was subsequently achieved by heated electrospray ionization facilitated by the HESI-II probe (Thermo Scientific) using the positive ion polarity mode, and a spray voltage of 3.5 kV. The sheath gas flow rate was 48 units with an auxiliary gas flow rate of 11 units, and a sweep gas flow rate of 2 units. The capillary temperature was 256°C and the auxiliary gas heater temperature was 413°C. The stacked-ring ion guide (S-lens) radio frequency level was at 90 units. Mass spectra were recorded with the QExactive mass spectrometer (Thermo Scientific), and data analysis was performed with the Thermo Xcalibur Qual Browser. Standard curves generated for ATP, NAD^+ and NADH were used as reference for metabolite quantification.

Flow cytometry

Cells were fixed with 1.6% PFA, permeabilized with ice-cold 90% methanol and blocked using a buffer containing 0.3M glycine, 5% goat serum and 1% bovine serum albumin (BSA) in PBS. For cell lineage characterization, iPSCs were stained for pluripotency markers using mouse anti-Oct4 (Santa Cruz, cat. no. sc-5279 AF488, 1:100), rabbit anti-Nanog (Abcam, cat. no. ab80892, 1:100), mouse anti-SSEA4 (R&D Systems, cat. no. FAB1435A, 1:20), mouse anti-Tra-1-60 (Stem Cell Technologies, cat. no. 60064PE, 1:20) and mouse anti-Tra-1-81 (Stem Cell Technologies, cat. no. 60065AZ, 1:20). NSCs were characterized using mouse anti-PAX6 (Novus Biologicals,

cat. no. NBP2-34705APC, 1:50), mouse anti-Nestin (R&D Systems, cat. no. IC1259P, 1:200) and mouse anti-SOX2 (R&D Systems, cat. no. IC2018G, 1:100). Characterization of astrocytes were conducted using the following antibodies: mouse anti-GFAP (BD Biosciences, cat. no. 561470, 1:5), mouse anti-CD44 (BD Biosciences, cat. no. 555476, 1:50), rabbit anti-EAAT1 (Abcam, cat. no. ab416, 1:100), rabbit anti-S100β (Abcam, cat. no. ab196442, 1:100) and mouse anti-GS (Abcam, cat. no. ab64613, 1:100). For TFAM and TOMM20 expression, cells were stained with anti-TFAM antibody conjugated with Alexa Fluor® 488 (Abcam, cat. no. ab198308, 1:400) and anti-TOMM20 antibody conjugated with Alexa Fluor® 488 (Santa Cruz Biotechnology, cat. no. sc 17764 AF488, 1:400), separately. Staining of MRC complexes was conducted using the primary antibodies anti-NDUFB10 (Abcam, cat. no. ab196019, 1:1000), anti-SDHA [2E3GC12FB2AE2] (Abcam, cat. no. ab14715, 1:1000) and anti-COX IV [20E8C12] (Abcam, cat. no. ab14744, 1:1000), followed by secondary antibody incubation (1:400). All samples were immediately analyzed on a BD Accuri™ C6 flow cytometer and Accuri™ C6 software was used for data analysis. Gating of cells was conducted from dot plots of SSC-H/SSC-A and FSC-H/FSC-A to exclude doublets. For each sample, more than 10,000 events were recorded.

Quantification of mtDNA copy number

Total DNA was extracted using a QIAGEN DNeasy Blood and Tissue Kit (QIAGEN, cat. no. 69504) according to the manufacturer's protocol. Assessment of mtDNA copy number was performed using quantitative PCR (qPCR) as previously described [11]. ND1 and APP was amplified using the primers described in Table S2.

Western blotting

Extraction of protein was performed using 1X RIPA lysis buffer (Sigma-Aldrich, cat. no. R0278) supplemented with Halt™ Protease and Phosphatase Inhibitor Cocktail (Invitrogen, cat. no. 78444). Protein concentration was determined using BCA protein assay (Thermo Fisher Scientific, cat. no. 23227). The cell protein was loaded into NuPAGE™ 4-12% Bis-Tris Protein Gels (Invitrogen, cat. no. NP0321PK2), and resolved in PVDF membrane (Bio-Rad, cat. no. 1704157) using the Trans-Blot® Turbo™ Transfer System (Bio-Rad, Denmark). Membranes were blocked with 5% non-fat dry milk or 5% BSA in TBST for 1 h at RT. Membranes were then incubated overnight at 4°C with rabbit monoclonal IgG anti-PGC-1α (1:1000, Abcam, cat. no. ab77210), rabbit polyclonal IgG anti-p-SIRT1 (Ser47) (1:2000, Cell Signaling Technology, cat. no. 2314), rabbit polyclonal IgG anti-PINK1 (1:500, Proteintech, cat. no. 23274-1-AP), rabbit polyclonal IgG anti-Parkin (1:500, Proteintech, cat. no. 14060-1-AP), rabbit polyclonal IgG anti-LC3B (1:3000, Abcam, cat. no. ab51520), rabbit monoclonal anti-SQSTM1/p62 (1:10000, Abcam, cat. no. ab109012), rabbit monoclonal IgG anti-p-ULK1 (Cell Signaling Technologies, cat. no. 8054, 1:1000) and mouse monoclonal IgG anti-GAPDH (1:5000, Abcam, cat. no. ab8245) as a loading control. After washing in TBST, membranes were incubated with donkey Anti-mouse monoclonal antibody or swine anti-rabbit monoclonal antibody conjugated to HRP secondary antibody (Jackson Immunoresearch, 1:1000), for 1 h at RT. Super signal west Pico chemiluminescent substrate (Thermo Fisher Scientific, cat. no. 34577) was used as enzyme substrate according to manufacturer's recommendations. The membranes were visualized in SynGene scanner (VWR, USA).

Data analysis

In order to minimize the phenotypic diversity caused by intra-clonal heterogeneity, which is a common issue for iPSC-related studies, multiple clones from each line were included in all analyses and more than 3 biological repeats were conducted for each clone to ensure adequate power to detect a pre-specified effect size. Data was presented as mean ± standard error of the mean (SEM) for the number of samples (n≥3 per clone, Table S3). Distributions were tested for normality using the Shapiro-Wilk test and outliers detected using the ROUT method (Q=1%). Mann-Whitney U test was used to assess statistical significance for variables with non-normal distribution, while unpaired student's t-test was applied for normal distributed variables. Welch's t-test was used for parametric data without equal variances. Data was analyzed and figures were produced by GraphPad Prism software (Prism 8.0, GraphPad Software, Inc.). Significance was denoted for P values of less than 0.05.

Results

ESCs and iPSCs show similar cell pluripotency and mitochondrial function.

We generated iPSCs from two control human fibroblast lines, Detroit 551 and AG05836, which were reprogrammed via retroviral induction or through Sendai virus vectors as described previously [12]. Three human embryonic stem cells (ESC) were used - line 429 (ESC1), line 360 (ESC2) and H1 (ESC3). The number of technical and biological replicates used in the study can be found in Table S3. All iPSC lines and ESC lines displayed similar morphology with well-defined sharp edges and contained tightly packed cells (Fig. 1A). Next, we characterized their pluripotency using immunostaining and flow cytometry for protein expression and RT-qPCR analysis for gene expression level. Immunostaining confirmed that all iPSCs and ESCs expressed the specific pluripotent markers Oct4, SOX2 (Fig. 1A & S3) and SSEA4 (Fig. S3). RT-qPCR analysis showed no significant difference in the mRNA expression levels of *LIN28A*, *NANOG*, and *POU5F1* between iPSCs and ESC lines (Fig. 1B). Flow cytometric analysis of the expression levels of Oct4, Nanog and pluripotent surface markers SSEA4, TRA-1-60 and TRA-1-81 showed that ESC and iPSC lines exhibited similar levels of pluripotent marker expression (Fig. 1C).

After confirming that ESCs and iPSCs displayed comparable pluripotent characteristics, we investigated mitochondrial function and mass. First, we applied flow cytometry to investigate mitochondrial mass and MMP by double staining cells with MTG and TMRE. In order to understand the relationship between MMP and the volume of mitochondria present in live cells, we divided the measured fluorescence intensity of TMRE by MTG to get MMP per mitochondrial mass. The ratio TMRE/MTG gives a relative measure of MMP independent of mitochondrial mass that we call specific MMP. ESC and iPSC lines showed no differences in mitochondrial mass measured by MTG (Fig. 1D) or specific MMP (Fig. 1E). Next, we measured ATP production by luminescence assay, but no significant difference in ATP levels were found in iPSCs compared to ESCs (Fig. 1F).

Further, we investigated mtDNA copy number using two approaches: first, with flow cytometry to assess the level of TFAM, which binds mtDNA in molar quantities and second, using qPCR. For flow cytometric quantification we ratioed TFAM against TOMM20 to correlate TFAM levels to mitochondrial mass. No significant difference was detected in Total TFAM (Fig. 1G) or TFAM levels corrected for mitochondrial content between ESCs and iPSC lines (Fig. 1H). Quantification of mtDNA copy number by qPCR, which relates mitochondrial *ND1* to the nuclear *APP* gene, also showed no

difference between ESC and iPSC lines (Fig. 1I).

To examine MRC proteins, we measured expression of MRC complex I subunit NDFUB10, complex II subunit SDHA and complex IV subunit COXIV using flow cytometry. Again, these values were correlated to the amount of TOMM20 as a measure of mitochondrial mass. We found similar levels of complex I (Fig. 1J), II (Fig. 1K) and IV (Fig. 1L) in ESCs and iPSCs.

IPSC-derived NSCs have lower ATP production and complex IV expression compared to ESC-derived NSCs.

We generated NSCs from ESCs and iPSCs and compared the mitochondrial function in these cells. NSCs (Fig. 2A) were derived using a modified dual SMAD protocol described previously [12]. Briefly, neural induction was initiated in which iPSCs or ESCs (Fig. 2A, a) progressed to a neural epithelial stage exhibiting clear neural rosette structures (Fig. 2A, b). After 5 days, neural spheres were generated by lifting neural epithelium and plating in suspension culture (Fig. 2A, c). Thereafter, NSCs were produced by dissociating neural spheres into single cells before subsequent re-plating in monolayers (Fig. 2A, d).

NSCs in monolayers showed a clear neural progenitor appearance (Fig. 2A, d). We confirmed the expression of specific lineage markers at different stages of neural induction using immunostaining: iPSCs showed Oct4 expression (Fig. 2A, e); neural epithelial cells showed rosette structures that uniformly expressed SOX2 (Fig. 2A, f); neurospheres showed positive PAX6 expression (Fig. 2A, g) and NSCs stained positively for Nestin (Fig. 2A, h). Next, all NSC lines were characterized by immunostaining and flow cytometry to investigate expression of neural progenitor markers. While immunostaining demonstrated positive expression of PAX6 and Nestin (Fig. 2B), flow cytometric quantification showed that iPSC-NSCs had lower expression of Nestin compared to ESC-NSCs, whereas the PAX6 level was found to be similar (Fig. 2C).

We applied the same experimental approaches to investigate mitochondrial function in NSCs as was used in iPSCs. Mitochondrial mass measured by MTG (Fig. 2D) and specific MMP (Fig. 2E) calculated by TMRE/MTG showed no differences between ESC-NSCs and iPSC-NSCs. However, measurements of intracellular ATP production by luminescence assay revealed that ATP level was decreased in iPSC-NSCs (Fig. 2F). Next, we assessed the level of TFAM in both sets of NSCs. While a significant difference in total TFAM level was found (Fig. 2G), when adjusted for mitochondrial mass (TFAM/TOMM20), no difference was observed between iPSC-NSCs and ESC-NSCs (Fig. 2H). This indicated a similar level of mtDNA copy number, which was further confirmed by qPCR (Fig. 2I). Flow cytometric analysis showed ESC-NSCs and iPSC-NSCs had similar levels of complex I (Fig. 2J) and II (Fig. 2K) normalized to TOMM20, however, we observed a significantly decreased level of complex IV per TOMM20 in iPSC-NSCs compared to ESC-NSCs (Fig. 2L).

Mitochondrial function and biogenesis in iPSC-astrocytes appears greater than in ESC-astrocytes.

Astrocytes have a variety of functions in the central nervous system including metabolic support of neurons. To generate astrocytes, we used the protocol described in our previous studies [12]. We succeeded in generating astrocytes with stellate

morphology from both iPSC-NSCs and ESC-NSCs (Fig. 3A, a & f). Further, we characterized all astrocytes by immunostaining using a panel of astrocytic lineage markers including glial fibrillary acidic protein (GFAP) and CD44, and the functional markers excitatory amino acid transporter 1 (EAAT-1) and glutamine synthetase (GS). All astrocytes showed positive expression of GFAP (Fig. 3A, b & g), CD44, EAAT-1 and GS [12], and no evident contamination of neurons as assessed by immunostaining with anti-double cortin (DCX) (Fig. 3A, c & h). After we confirmed astrocytic identity, we used flow cytometry to assess the purity and protein expression. All astrocytes displayed over 90% positive populations for GFAP, CD44, EAAT-1, S100β and GS (Fig. S1). While GFAP expression was found to be significantly higher in iPSC-astrocytes, no difference in expression was discovered between ESC-astrocytes and iPSC-astrocytes for the other astrocytic lineage markers (Fig. 3B).

We next compared mitochondrial function in ESC- and iPSC-astrocytes using the same approach as above. We observed that both sets of astrocytes showed similar MTG level (Fig. 3C) and specific MMP calculated by TMRE/MTG (Fig. 3E), though total MMP level, measured by TMRE alone (Fig. 3D), was significantly increased in iPSC-astrocytes. While ATP production measured by luminescence assay showed no significance between ESC-astrocytes and iPSC-astrocytes (Fig. 3F), measurements by LC-MS demonstrated higher ATP level in iPSC-astrocytes (Fig. 3G). Furthermore, we investigated the calcium level (Rhod-2-AM) by flow cytometry, but no significant difference was found (Fig. 3H).

Next, we examined mtDNA both indirectly using TFAM and directly using qPCR. Flow cytometry showed that while total TFAM expression (Fig. S4, A) was similar, specific TFAM level (Fig. 3I) was higher in iPSC-astrocytes versus ESC-astrocytes, though this did not reach significance. However, a significant increase in TFAM level was found by western blotting (Fig. S4), indicating increased mtDNA in iPSC-astrocytes. This was further confirmed by qPCR showing a significantly higher ND1/APP ratio in iPSC-astrocytes than ESC-astrocytes (Fig. 3J). When we measured mitochondrial complex subunit expression, we found no significant difference between ESC-astrocytes and iPSC-astrocytes for both total and specific complex I and complex II levels (Fig. 3K, 3L, 3O & 3P). However, an increase in total and specific complex IV in iPSC-astrocytes was observed (Fig. 3M & N), though this was only significant for specific complex IV (Fig. 3N). Considering that maintenance of the NAD^+/NADH ratio is vital for mitochondrial function, we measured NAD^+ and NADH levels using LC-MS. While levels of NAD^+ and NADH were similar in both sets of astrocytes (Fig. 4B & C), a significant increase in the NAD^+/NADH ratio was found in iPSC-astrocytes (Fig. 4A).

As the MRC is a major source of intracellular ROS, we studied ROS production by dual staining with DCFDA and MTDR. Measurements of Total ROS (DCFDA) production showed an increase in iPSC-astrocytes compared to ESC-astrocytes (Fig. 4D). To assess ROS level related to mitochondrial volume, we divided Total ROS by a measure of MTDR to give specific ROS and again found a higher specific ROS level in iPSC-astrocytes (Fig. 4E). To confirm that the increased ROS was of mitochondrial origin, we used the mito-ROS sensitive fluorescent dye MitoSOX Red and quantified both Total mito-ROS and the ratio of mito-ROS to mitochondrial volume defined by MTG. Again, iPSC-astrocytes showed a significant increase in the mean intensity of MitoSOX Red fluorescence at Total mito-ROS levels (Fig. 4F). However, no significant difference was found after normalizing MitoSox to mitochondrial mass (MTG) (Fig. 4G).

Next, we investigated relevant molecular proteins involved in these biological changes, including peroxisome proliferator-activated receptor-gamma (PPAR-γ) coactivator-1 alpha (PGC-1α), a positive regulator of mitochondrial biogenesis and respiration [13]. Sirtuin 1 (SIRT1) is in a protein complex with PGC-1α, and functions as a sensor for nutrient fluctuations via NAD^+ and regulates PGC-1α-dependent gene expression [14]. From western blotting, we found upregulation of PGC-1α and p-SIRT1 in iPSC-astrocytes compared to ESC-astrocytes (Fig. 4H & I, a & b). However, this did not lead to an increase in mitochondrial mass, as evidenced by MTG (Fig. 3C), VDAC1 and TOMM20 (Fig. S4B, D & E).

These data suggest that iPSC-astrocytes exhibited greater levels of mitochondrial activity (ATP, NAD^+/NADH, mtDNA) and mitochondrial biogenesis (PGC-1α). This is opposite from what was found in NSCs.

IPSC-astrocytes exhibited no changes in autophagy compared to ESC-astrocytes.

Based on our data suggesting that iPSC-astrocytes showed enhanced mitochondrial function and biogenesis compared to ESC-astrocytes, we explored whether astrocytes derived from iPSCs showed more active autophagy. We used western blotting to quantify the level of autophagy-related proteins including autophagosome marker microtubule-associated protein 1 light chain 3β (LC3B), autophagy receptor p62 and phosphorylated unc-51 like autophagy activating kinase 1 (p-ULK1) using western blotting. Our results showed no significant differences in LC3B-II/LC3B-I (Fig. 4J & K, a), p62 (Fig. 4J & K, b) and p-ULK1 (Fig. 4J & K, c) expression, indicating a similar degree of autophagy between ESC-astrocytes and iPSC-astrocytes. No difference in PINK1 and Parkin levels were found in iPSC-astrocytes compared to ESC-astrocytes (Fig. 4J & K, d & e).

These data indicate that while iPSC-astrocytes displayed increased mitochondrial biogenesis, this did not result from an increased autophagy.

Discussion

In this study, we compared ESCs and iPSCs at various stages from pluripotent to neural lineage precursors and glial astrocytes to ascertain if stem cell origin influenced mitochondrial function. At each stage, lineage identity was similar, yet subtle changes in mitochondrial function evolved as cells differentiated. Interestingly, these changes varied depending on cell type with NSCs showing decreased ATP production in iPSC-derived cells compared to ESC-derived cells, while the reverse was found in astrocytes. These results have implications for our understanding of how mitochondria are influenced and changed during development.

While the use of ESCs is restricted, iPSCs are widely used to study all types of human disease [12, 15, 16]. Nevertheless, ESCs remain the “gold standard” and we, and others use these cells to control for lineage development and often as controls for functional studies on the assumption that the two cell types are equivalent. This question has not, however, been fully evaluated. To address this, we compared multiple mitochondrial parameters including mitochondrial volume and membrane potential, MRC complexes, ATP production, NAD^+, NADH and the redox ratio and mtDNA copy number in ESCs and iPSCs at the pluripotent stage and during differentiation to neural lineage cells

including NSCs and astrocytes.

In our experiments, both iPSCs and ESCs were indistinguishable morphologically and showed similar expression of relevant markers at the pluripotent stage. Interestingly, previous studies have shown some differences between these cell types: one study demonstrated minor differences in chromatin and gene expression but concluded that iPSCs did not form a different new class of pluripotent stem cell [17]. The same conclusion was made by Chin et al [5] who found a small panel of differentially expressed genes between iPSC and ESC lines, but these could not be categorized by gene ontology analysis to the same functional group. It appears, therefore, that iPSCs do not represent a different class of pluripotent stem cells than ESCs.

When we looked at mitochondrial parameters in ESCs and iPSCs, we found that mitochondrial volume, membrane potential, level of MRC complexes and mtDNA copy number were similar. We concluded, therefore, that at the pluripotent stage, iPSCs and ESCs were similar in several aspects of their mitochondrial function. This finding is consistent with a previous study by Choi et. al., who showed that iPSCs and ESCs were largely similar in both mitochondrial morphology and in a greater reliance on glycolysis [18].

Mitochondrial function also appeared similar in NSCs derived from both stem cell types; however, we did observe a significant reduction in ATP production and lower complex IV expression in these neuronal precursors. A trend towards lower complex IV was seen in iPSCs, but whether changes in the amount of complex IV reflect differences in the stoichiometry or super-complex construction of the MRC in iPSC-derived cells, is unclear. This result indicates that while mitochondrial function at the ESC and iPSC stage are comparable, there are subtle differences that might be exacerbated during mitochondrial remodeling induced by reprogramming and differentiation [18]. Our study suggests that iPSCs, and their derived NSCs are more glycolytic than ESCs and their derivatives, and that this occurs despite apparent morphological maturation.

Interestingly, our study clearly showed that iPSC-astrocytes differed in their mitochondrial activity and biogenesis when compared to ESC-astrocytes. iPSCs-astrocytes displayed higher total MMP and ATP levels, increased mtDNA copy number evidenced by both TFAM expression and ND1/APP, as well as elevated complex IV expression. That these changes reflect greater metabolic activity was supported by a higher redox ratio (NAD^+/NADH) and increased ROS production. These findings suggest that the dynamic changes in number and respiratory capacity of mitochondria, and in metabolic regulation associated with cellular differentiation are different in astrocytes and NSCs. This may be due to the differing metabolic requirements in astrocytes and neural cells since astrocytes primarily generate ATP via anaerobic glycolysis and are net lactate exporters, whereas neurons require high levels of aerobic mitochondrial metabolism [19].

As a corollary to the metabolic changes in mitochondria, we found upregulation of the PGC-1α /SIRT1 pathway in iPSC astrocytes compared to ESC-derived cells. PGC-1α has been identified as a transcriptional coactivator and metabolic regulator involved in the adaptation of tissue-specific metabolic pathways in response to environmental and nutritional stimuli [20]. Previous studies identified that SIRT1 functionally interacts with PGC-1α [21]. This interaction and deacetylation of PGC-1α by SIRT1 could be mediated

by energy fluctuations and nutrient levels, and in turn, lead directly to transcriptional changes of metabolic enzymes and pathways [22]. Thus, we conclude in our study that the metabolic adaptations observed in iPSC-derived astrocytes might be regulated through the PGC-1α and SIRT1 pathways. However, no differences in mitochondrial mass or autophagy was observed, suggesting a possible increase in the turnover of mitochondrial protein content, though this will have to be further explored. Recent work highlighted that PGC-1α also plays a role in the regulation of mitochondrial density in neuronal cells through enhancing mitochondrial biogenesis [23] and that the involvement of PGC-1α in the formation, maintenance and reorganization of synapses are critical for brain development [24]. Therefore, our study supports that PGC-1α may regulate mitochondrial function and maintenance in astrocytes through augmentation of mitochondrial biogenesis.

Our study found differences in mitochondrial function between iPSCs and ESCs during differentiation into neural cells. This illustrates a specific aspect of the differences between ESC disease models and iPSC-based models that should be considered when choosing between ESCs or iPSCs and other mitochondria-related disease models. One reason for these observed changes may be that the iPSC reprogramming process itself may add "noise" to the system, something which might not be detected at the pluripotent stage but can possibly influence cellular function after differentiation. While this might be avoided using ESCs, a general advantage of iPSC-based models compared to ESC-based models is that selected patients already exhibit mutation-related phenotypes. This ensures that the specific genetic background has no effect on the penetrance of the mutation. Considering the potential differences between iPSCs and ESCs at different stages of differentiation, a more robust model might be a "combinatorial approach" of both ESCs genetically engineered to carry specific mutations and patient-derived iPSCs, as have recently been conducted for Fanconi anemia [25] and long QT syndrome [26]. However, in some cases only one of these two approaches is feasible, e.g., the use of iPSCs over ESCs in modeling of multigenic disorders where the genetic factor cannot be pinpointed to a single gene [27].

In summary, our study shows that iPSCs and ESCs have similar mitochondrial profiles when in the pluripotent state, but during further differentiation, differences in mitochondrial activity emerge and these vary according to cell type. Moreover, this highlights the functional differences that can occur between iPSCs and ESCs during differentiation into specific cell types, which should be taken into account when using these cell types, and their differentiated derivatives, in disease modeling.

Data Availability Statement: All raw data in this study are available upon request.

Ethical approval

The project was approved by the Western Norway Committee for Ethics in Health Research (REK nr. 2012/919); the study was performed in accordance with the Declaration of Helsinki.

Competing interests

The authors declare that they have no competing interests.

Funding

This work was supported by funding from the Norwegian Research Council (project number: 229652), Rakel og Otto Kr.Bruuns legat. G.J.S was partly supported by the Norwegian Research Council through its Centre of Excellence funding scheme (project number: 262613).

Author's contributions

K.L and L.A.B contributed to the conceptualization; K.L, C.K.K and A.C contributed to the methodology; K.L, A.C, C.K.K, L.E.H performed the investigations; C.K.K. and A.C wrote the original draft. All the authors contributed to writing, reviewing, and editing. C.K.K and A.C contributed to the statistical analysis; L.A.B and G.J.S contributed to the funding acquisition; G.J.S, M.Z. and L.A.B contributed to providing the resources; K.L contributed to the supervision.

All authors agree to the authorship.

Acknowledgements

We thank members of the Molecular Imaging Centre and Flow Cytometry Core Facility for their expertise and assistance in confocal imaging and flow cytometry data recording.

Figure Legends:

Figure 1: ESCs and iPSCs show similar cell pluripotency and mitochondrial function.

A: Representative brightfield images and confocal images of immunofluorescence staining of stem cell markers Oct4 and SOX2 in ESCs and iPSCs. Nuclei are stained with DAPI (blue) (Scale bar, 50 µm or 100 µm).

B: RT-qPCR quantification of gene expression for *LIN28A*, *NANOG*, and *POU5F1* for ESCs and iPSCs. The gene expression of the individual clones is assessed by fold change using the comparative ΔΔCt method.

C: Flow cytometric analysis of expression level of pluripotency markers Oct4, Nanog, SSEA4, TRA-1-60 and TRA-1-81 in ESCs and iPSCs.

D & E: Flow cytometric analysis of MTG (D) and specific MMP (Total TMRE/MTG) (E).

F: Intracellular ATP production in ESC and iPSC lines.

G & H: Flow cytometric analysis of Total TFAM protein expression level (G) and specific TFAM (Total TFAM/TOMM20) expression (H) in ESCs and iPSCs.

I: Relative mtDNA copy number analyzed by qPCR for mitochondrial *ND1* relative to nuclear *APP* (ND1/APP) in ESC and iPSC lines.

J-L: Flow cytometric measurements of MRC complex I (J), II (K) and IV (L) protein level in ESC and iPSC lines. Expressed as specific complex I, II and IV level (Total complex I, II, IV level/TOMM20).

Data information: Data are presented as mean ± SEM for the number of samples.

Significance is denoted for P values of less than 0.05. Ns: no significance.

Figure 2: Characterization of NSCs and comparison of mitochondrial function in iPSC-NSCs and ESC-NSCs.

A: Representative brightfield images (upper panel) and immunostaining for specific stages (lower panel) during neural induction from iPSCs to NSCs. Upper panel displays the morphology in culture of different cell types during neural induction to NSCs from iPSCs including iPSCs (a); neuroepithelium with rosette-like structures (b); neural spheres with defined round shapes in suspension culture (c) and NSCs in monolayers (d) (scale bars, 50 µm). The lower panel demonstrates immunostaining corresponding to the specific stages in the upper panel: Oct4 (green) and SSEA4 (red) expression in iPSCs (e) (scale bar, 100 µm); SOX2 (red) expression in neuroepithelium (f) (scale bar, 50 µm); PAX6 (green) expression in neural spheres (g) (scale bar, 50 µm); Nestin (red) expression in NSCs (h) (scale bar, 50 µm).

B: Immunofluorescent labeling of NSC markers PAX6 (green) and Nestin (red) (scale bar, 50 µm) in neural spheres and NSCs from ESC and iPSC lines. Nuclei are stained with DAPI (blue).

C: Flow cytometric analysis of the expression level of pluripotency markers Nestin and PAX6 ($n \geq 3$, technical replicates per line for all) in ESC-NSCs and iPSC-NSCs.

D & E: Flow cytometric analysis of MTG (D) and specific MMP (TMRE/MTG) (E) in ESC-NSCs and iPSC-NSCs.

F: Intracellular ATP production in ESC-NSCs and iPSC-NSCs .

G, H: Flow cytometric analysis of Total TFAM expression level and specific TFAM (Total TFAM/TOMM20) expression in ESC-NSCs and iPSC-NSCs.

I: Relative mtDNA copy number analyzed by qPCR for mitochondrial *ND1* relative to nuclear *APP* (ND1/APP) in ESC-NSCs and iPSC-NSCs.

J-L: Flow cytometric measurements of MRC complex I, II and IV protein level in ESC-NSCs and iPSC-NSCs. Expressed as specific complex I, II and IV level (Total complex I, II, IV level/TOMM20).

Data information: Data are presented as mean ± SEM for the number of samples. Significance is denoted for P values of less than 0.05. * $P<0.05$; ** $P<0.01$; ns: no significance.

Figure 3: Characterization of astrocytes and comparison of mitochondrial function in iPSC-astrocytes and ESC-astrocytes.

A: Representative brightfield images displaying the morphology of ESC- and iPSC-astrocytes in culture (a & f), expression of GFAP (red) (b & g), DCX (green) (c &h) and DAPI (blue) (c & h) by immunostaining, and merged images (d & i) (scale bar, 50 µm or 25 µm).

B: Flow cytometric analysis of expression level of astrocyte markers GFAP, CD44, EAAT-1, and GS in Detroit 551 iPSC-astrocytes and ESC-astrocytes.

C & E: Flow cytometric analysis of MTG (C), Total MMP (TMRE) (D) and specific MMP (Total TMRE/MTG) (E) in ESC-astrocytes and iPSC-astrocytes.

F & G: Intracellular ATP production in ESC-astrocytes and iPSC-astrocytes measured by luminescence assay (F) and LC-MS (G).

H: Mitochondrial calcium concentration (Rhod-2-AM) in ESC-astrocytes and iPSC-astrocytes measured by flow cytometry.

I: Flow cytometric analysis specific TFAM (Total TFAM/TOMM20) protein expression (I) in ESC-astrocytes and iPSC-astrocytes.

J: Relative mtDNA copy number analyzed by qPCR for mitochondrial *ND1* in relation to nuclear *APP* (ND1/APP) in ESC-astrocytes and iPSC-astrocytes.

K-P: Flow cytometric measurements of MRC complex I (K & L), II (O & P) and IV (M & N) protein level in ESC-astrocytes and iPSC-astrocytes. Expressed as Total (K, M, O) and specific complex I (L), II (P) and IV (N) level (Total complex I, II, IV level/TOMM20).

Data information: Data are presented as mean ± SEM for the number of samples. Significance is denoted for P values of less than 0.05. * P<0.05; ** P<0.01; *** P<0.001; ns: no significance.

Figure 4: IPSC-astrocytes showed increased PGC-1α and p-SIRT1

A-C: LC-MS-based metabolomics for quantitative measurements of the NAD^+/NADH ratio (A), NAD^+ (B) and NADH (C) level in ESC-astrocytes and iPSC-astrocytes.

D-G: Flow cytometric measurements of intracellular ROS (D & E) and mito-ROS (F & G) production level in ESC-astrocytes and iPSC-astrocytes. Expressed as Total ROS (DCFDA) (D) and mito-ROS (MitoSOX Red) (F) or specific ROS (DCFDA/MTDR) (E) and mito-ROS (MitoSOX Red/MTG) (G).

H & I: Representative images (H) and quantification (I) for PGC-1α, p-SIRT1 and GAPDH by western blotting. Three independent experiments are included.

J & K: Representative images (J) and quantification (K) for LC3B-II/LC3B-I, p62, p-ULK1, PINK1, Parkin and GAPDH by western blotting. Three independent experiments are included.

Data information: Data are presented as mean ± SEM for the number of samples. Significance is denoted for P values of less than 0.05. * P<0.05; ** P<0.01; *** P<0.001; **** P<0.0001; ns: no significance.

References

1. Thomson JA, Itskovitz-Eldor J, Shapiro SS, Waknitz MA, Swiergiel JJ, Marshall VS, Jones JM. Embryonic stem cell lines derived from human blastocysts. Science 1998; 282:1145-7.
2. Takahashi K, Yamanaka S. Induction of pluripotent stem cells from mouse embryonic and adult fibroblast cultures by defined factors. Cell 2006; 126:663-76.

3. Marei HE, Althani A, Lashen S, Cenciarelli C, Hasan A. Genetically unmatched human iPSC and ESC exhibit equivalent gene expression and neuronal differentiation potential. Sci Rep 2017; 7:17504.
4. Boulting GL, Kiskinis E, Croft GF, Amoroso MW, Oakley DH, Wainger BJ, Williams DJ, Kahler DJ, Yamaki M, Davidow L, et al. A functionally characterized test set of human induced pluripotent stem cells. Nat Biotechnol 2011; 29:279-86.
5. Chin MH, Mason MJ, Xie W, Volinia S, Singer M, Peterson C, Ambartsumyan G, Aimiuwu O, Richter L, Zhang J, et al. Induced pluripotent stem cells and embryonic stem cells are distinguished by gene expression signatures. Cell Stem Cell 2009; 5:111-23.
6. Gore A, Li Z, Fung HL, Young JE, Agarwal S, Antosiewicz-Bourget J, Canto I, Giorgetti A, Israel MA, Kiskinis E, et al. Somatic coding mutations in human induced pluripotent stem cells. Nature 2011; 471:63-7.
7. Hussein SM, Batada NN, Vuoristo S, Ching RW, Autio R, Narva E, Ng S, Sourour M, Hamalainen R, Olsson C, et al. Copy number variation and selection during reprogramming to pluripotency. Nature 2011; 471:58-62.
8. Lister R, Pelizzola M, Kida YS, Hawkins RD, Nery JR, Hon G, Antosiewicz-Bourget J, O'Malley R, Castanon R, Klugman S, et al. Hotspots of aberrant epigenomic reprogramming in human induced pluripotent stem cells. Nature 2011; 471:68-73.
9. Stadtfeld M, Apostolou E, Akutsu H, Fukuda A, Follett P, Natesan S, Kono T, Shioda T, Hochedlinger K. Aberrant silencing of imprinted genes on chromosome 12qF1 in mouse induced pluripotent stem cells. Nature 2010; 465:175-81.
10. Siller R, Naumovska E, Mathapati S, Lycke M, Greenhough S, Sullivan GJ. Development of a rapid screen for the endodermal differentiation potential of human pluripotent stem cell lines. Sci Rep 2016; 6:37178.
11. Liang KX, Kristiansen CK, Mostafavi S, Vatne GH, Zantingh GA, Kianian A, Tzoulis C, Hoyland LE, Ziegler M, Perez RM, et al. Disease-specific phenotypes in iPSC-derived neural stem cells with POLG mutations. EMBO Mol Med 2020; 12:e12146.
12. Liang KX, Kianian A, Chen A, Kristiansen CK, Hong Y, Furriol J, Høyland LE, Ziegler M, Kråkenes T, Tzoulis C, et al. Stem cell derived astrocytes with POLG mutations and mitochondrial dysfunction including abnormal NAD+ metabolism is toxic for neurons. bioRxiv 2020:2020.12.20.423652.
13. Puigserver P, Spiegelman BM. Peroxisome proliferator-activated receptor-gamma coactivator 1 alpha (PGC-1 alpha): transcriptional coactivator and metabolic regulator. Endocr Rev 2003; 24:78-90.
14. Rodgers JT, Lerin C, Haas W, Gygi SP, Spiegelman BM, Puigserver P. Nutrient control of glucose homeostasis through a complex of PGC-1alpha and SIRT1. Nature 2005; 434:113-8.
15. Liang KX, Vatne GH, Kristiansen CK, Ievglevskyi O, Kondratskaya E, Glover JC, Chen A, Sullivan GJ, Bindoff LA. N-acetylcysteine amide ameliorates mitochondrial dysfunction and reduces oxidative stress in hiPSC-derived dopaminergic neurons with POLG mutation. Exp Neurol 2021; 337:113536.
16. Balafkan N, Mostafavi S, Schubert M, Siller R, Liang KX, Sullivan G, Bindoff LA. A method for differentiating human induced pluripotent stem cells toward functional cardiomyocytes in 96-well microplates. Sci Rep 2020; 10:18498.
17. Guenther MG, Frampton GM, Soldner F, Hockemeyer D, Mitalipova M, Jaenisch R, Young RA. Chromatin structure and gene expression programs of human embryonic and induced pluripotent stem cells. Cell Stem Cell 2010; 7:249-57.

18. Choi HW, Kim JH, Chung MK, Hong YJ, Jang HS, Seo BJ, Jung TH, Kim JS, Chung HM, Byun SJ, et al. Mitochondrial and metabolic remodeling during reprogramming and differentiation of the reprogrammed cells. Stem Cells Dev 2015; 24:1366-73.
19. Turner DA, Adamson DC. Neuronal-astrocyte metabolic interactions: understanding the transition into abnormal astrocytoma metabolism. J Neuropathol Exp Neurol 2011; 70:167-76.
20. Puigserver P, Wu Z, Park CW, Graves R, Wright M, Spiegelman BM. A cold-inducible coactivator of nuclear receptors linked to adaptive thermogenesis. Cell 1998; 92:829-39.
21. Nemoto S, Fergusson MM, Finkel T. SIRT1 functionally interacts with the metabolic regulator and transcriptional coactivator PGC-1{alpha}. J Biol Chem 2005; 280:16456-60.
22. Rodgers JT, Lerin C, Gerhart-Hines Z, Puigserver P. Metabolic adaptations through the PGC-1 alpha and SIRT1 pathways. FEBS Lett 2008; 582:46-53.
23. Wareski P, Vaarmann A, Choubey V, Safiulina D, Liiv J, Kuum M, Kaasik A. PGC-1{alpha} and PGC-1{beta} regulate mitochondrial density in neurons. J Biol Chem 2009; 284:21379-85.
24. Cheng A, Wan R, Yang JL, Kamimura N, Son TG, Ouyang X, Luo Y, Okun E, Mattson MP. Involvement of PGC-1alpha in the formation and maintenance of neuronal dendritic spines. Nat Commun 2012; 3:1250.
25. Liu GH, Suzuki K, Li M, Qu J, Montserrat N, Tarantino C, Gu Y, Yi F, Xu X, Zhang W, et al. Modelling Fanconi anemia pathogenesis and therapeutics using integration-free patient-derived iPSCs. Nat Commun 2014; 5:4330.
26. Bellin M, Casini S, Davis RP, D'Aniello C, Haas J, Ward-van Oostwaard D, Tertoolen LG, Jung CB, Elliott DA, Welling A, et al. Isogenic human pluripotent stem cell pairs reveal the role of a KCNH2 mutation in long-QT syndrome. EMBO J 2013; 32:3161-75.
27. Halevy T, Urbach A. Comparing ESC and iPSC-Based Models for Human Genetic Disorders. J Clin Med 2014; 3:1146-62.

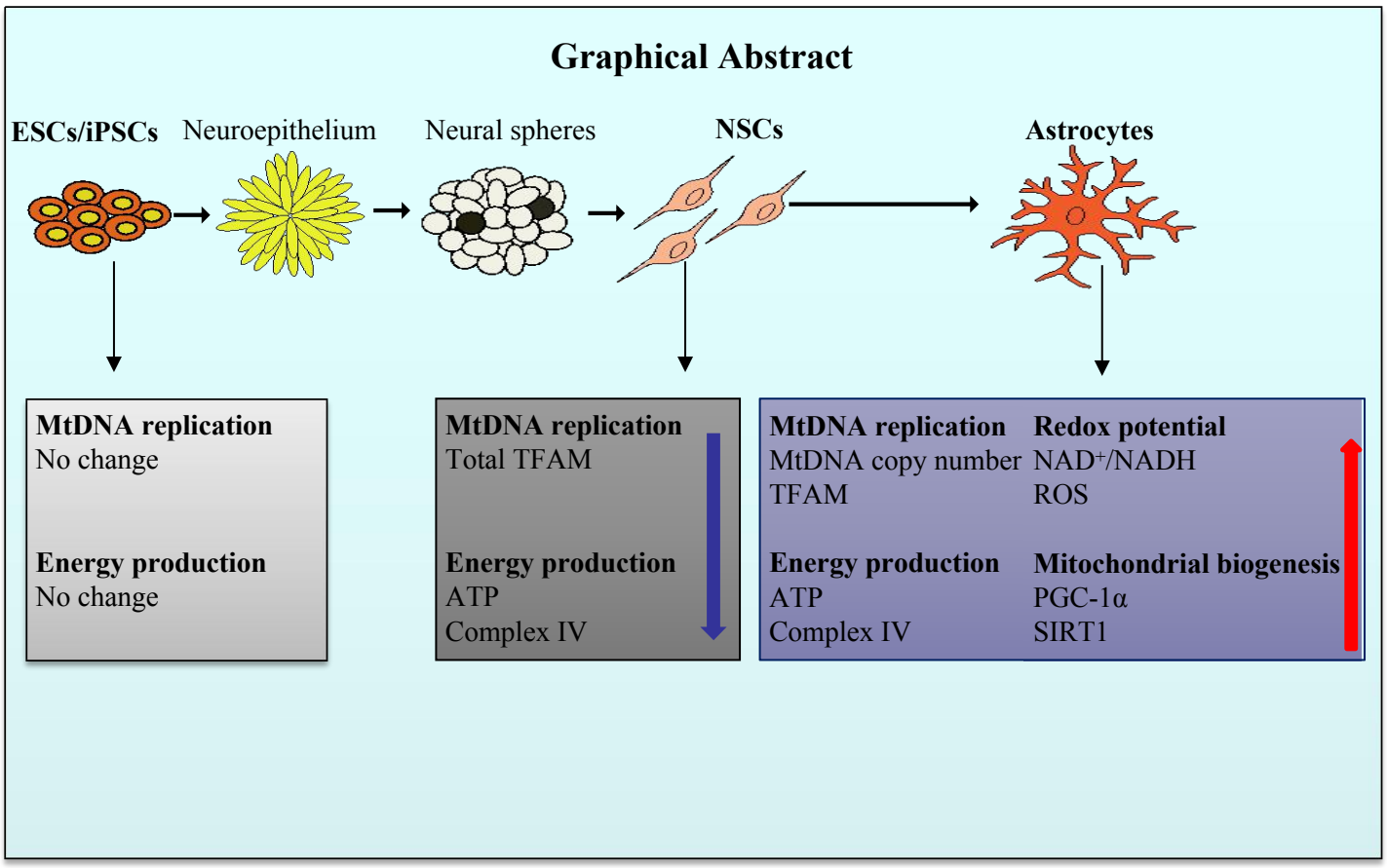

Figure 1

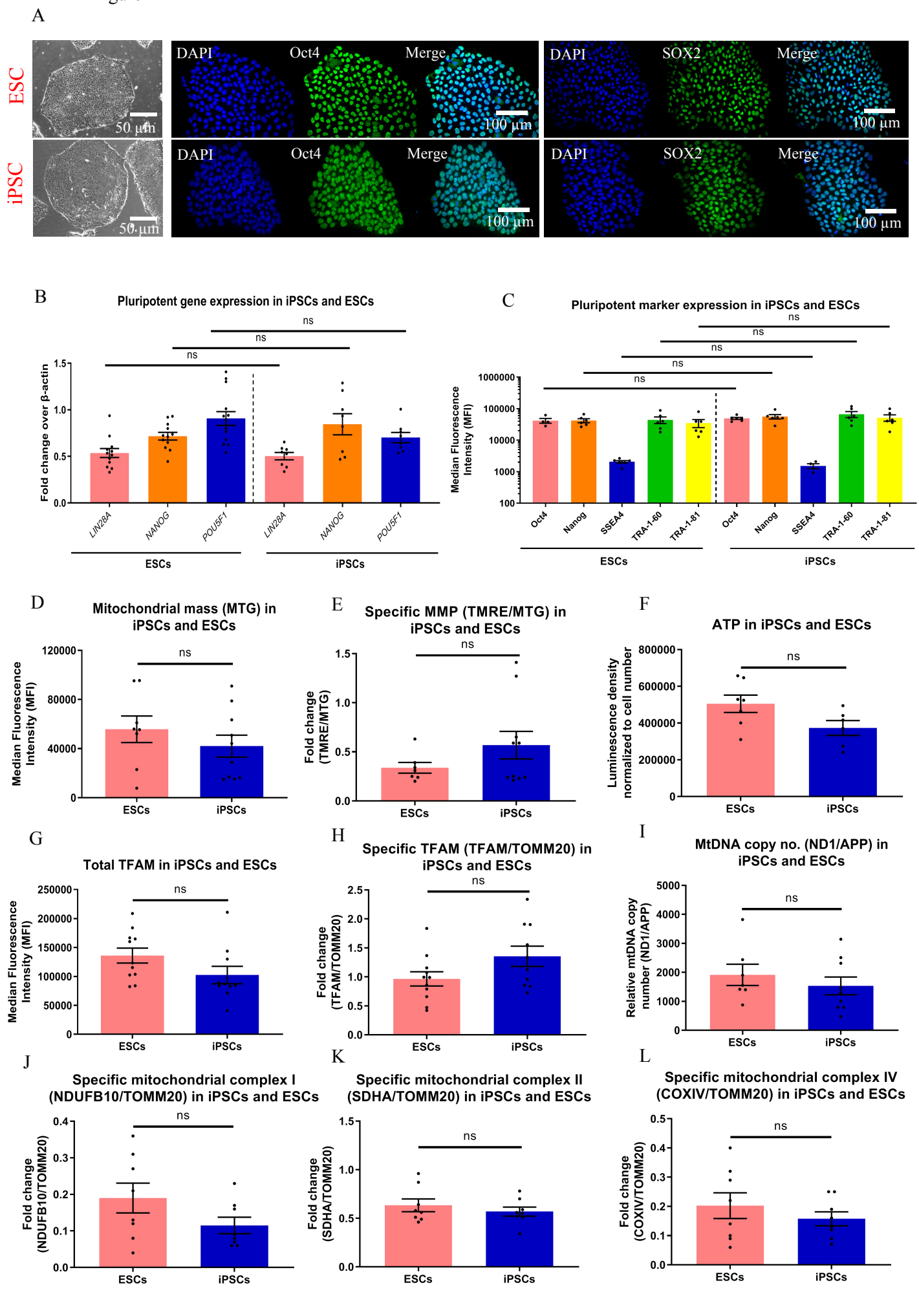
A
ESC
iPSC
DAPI
Oct4
Merge
SOX2
50 μm
100 μm
B
Pluripotent gene expression in iPSCs and ESCs
Fold change over β-actin
LIN28A
NANOG
POU5F1
ESCs
iPSCs
ns
C
Pluripotent marker expression in iPSCs and ESCs
Median Fluorescence Intensity (MFI)
Oct4
Nanog
SSEA4
TRA-1-60
TRA-1-81
D
Mitochondrial mass (MTG) in iPSCs and ESCs
E
Specific MMP (TMRE/MTG) in iPSCs and ESCs
Fold change (TMRE/MTG)
F
ATP in iPSCs and ESCs
Luminescence density normalized to cell number
G
Total TFAM in iPSCs and ESCs
H
Specific TFAM (TFAM/TOMM20) in iPSCs and ESCs
Fold change (TFAM/TOMM20)
I
MtDNA copy no. (ND1/APP) in iPSCs and ESCs
Relative mtDNA copy number (ND1/APP)
J
Specific mitochondrial complex I (NDUFB10/TOMM20) in iPSCs and ESCs
Fold change (NDUFB10/TOMM20)
K
Specific mitochondrial complex II (SDHA/TOMM20) in iPSCs and ESCs
Fold change (SDHA/TOMM20)
L
Specific mitochondrial complex IV (COXIV/TOMM20) in iPSCs and ESCs
Fold change (COXIV/TOMM20)

Figure 2

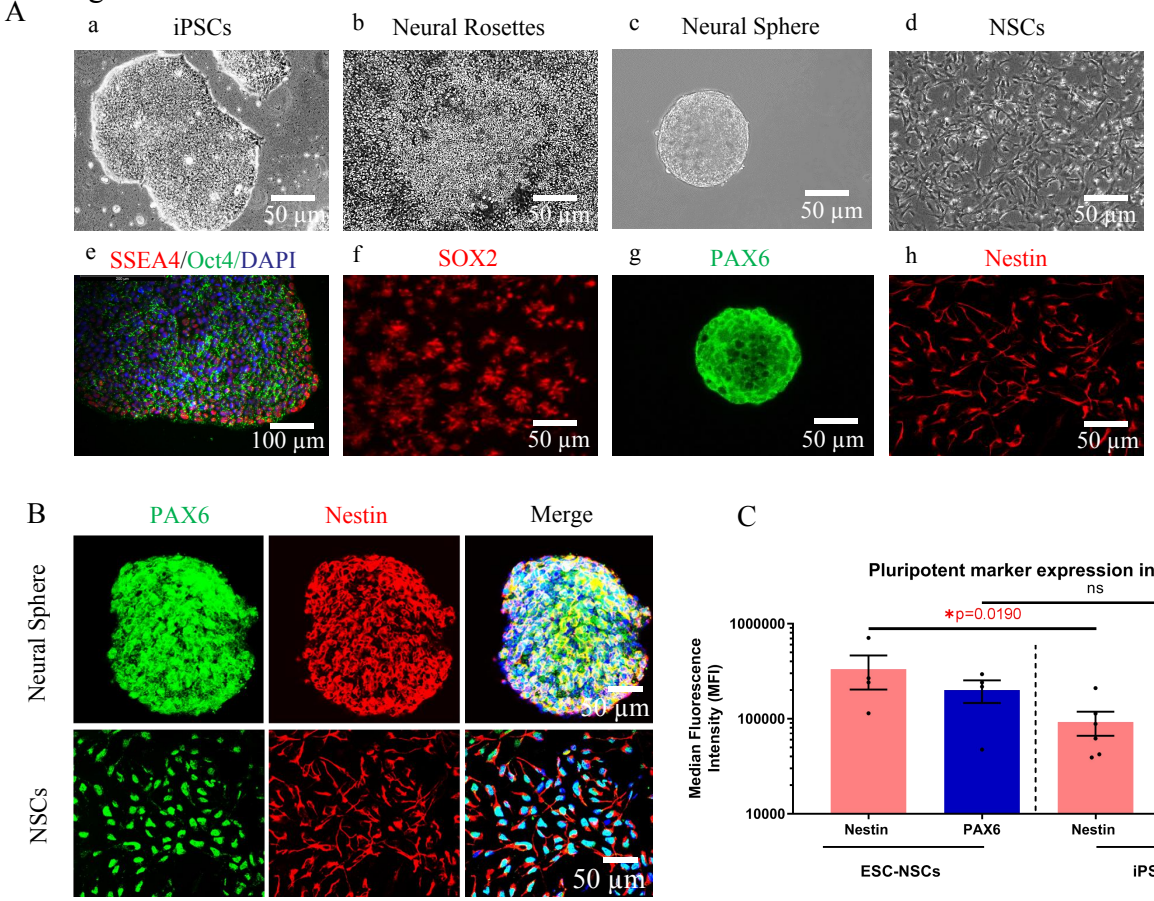
A
a iPSCs
b Neural Rosettes
c Neural Sphere
d NSCs
50 μm
e SSEA4/Oct4/DAPI
f SOX2
g PAX6
h Nestin
100 μm
B
PAX6
Nestin
Merge
Neural Sphere
NSCs
C
Pluripotent marker expression in NSCs
ns
*p=0.0190
Median Fluorescence Intensity (MFI)
1000000
100000
10000
Nestin
PAX6
Nestin
PAX6
ESC-NSCs
iPSC-NSCs

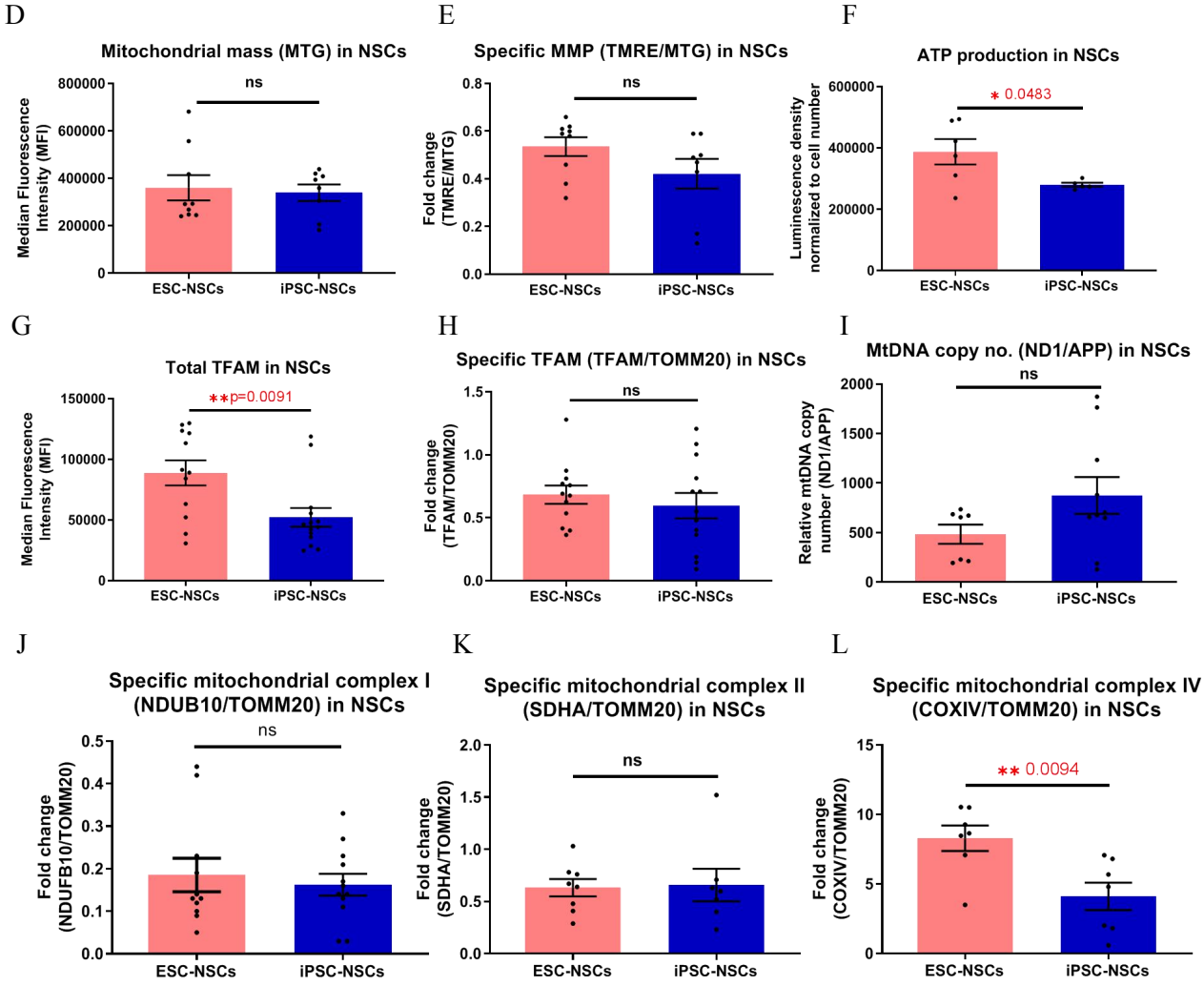
D
Mitochondrial mass (MTG) in NSCs
ns
Median Fluorescence Intensity (MFI)
800000
600000
400000
200000
0
ESC-NSCs
iPSC-NSCs
E
Specific MMP (TMRE/MTG) in NSCs
ns
Fold change (TMRE/MTG)
0.8
0.6
0.4
0.2
0.0
ESC-NSCs
iPSC-NSCs
F
ATP production in NSCs
* 0.0483
Luminescence density normalized to cell number
600000
400000
200000
0
ESC-NSCs
iPSC-NSCs
G
Total TFAM in NSCs
**p=0.0091
Median Fluorescence Intensity (MFI)
150000
100000
50000
0
ESC-NSCs
iPSC-NSCs
H
Specific TFAM (TFAM/TOMM20) in NSCs
ns
Fold change (TFAM/TOMM20)
1.5
1.0
0.5
0.0
ESC-NSCs
iPSC-NSCs
I
MtDNA copy no. (ND1/APP) in NSCs
ns
Relative mtDNA copy number (ND1/APP)
2000
1500
1000
500
0
ESC-NSCs
iPSC-NSCs
J
Specific mitochondrial complex I (NDUB10/TOMM20) in NSCs
ns
Fold change (NDUFB10/TOMM20)
0.5
0.4
0.3
0.2
0.1
0.0
ESC-NSCs
iPSC-NSCs
K
Specific mitochondrial complex II (SDHA/TOMM20) in NSCs
ns
Fold change (SDHA/TOMM20)
2.0
1.5
1.0
0.5
0.0
ESC-NSCs
iPSC-NSCs
L
Specific mitochondrial complex IV (COXIV/TOMM20) in NSCs
** 0.0094
Fold change (COXIV/TOMM20)
15
10
5
0
ESC-NSCs
iPSC-NSCs

Figure 3

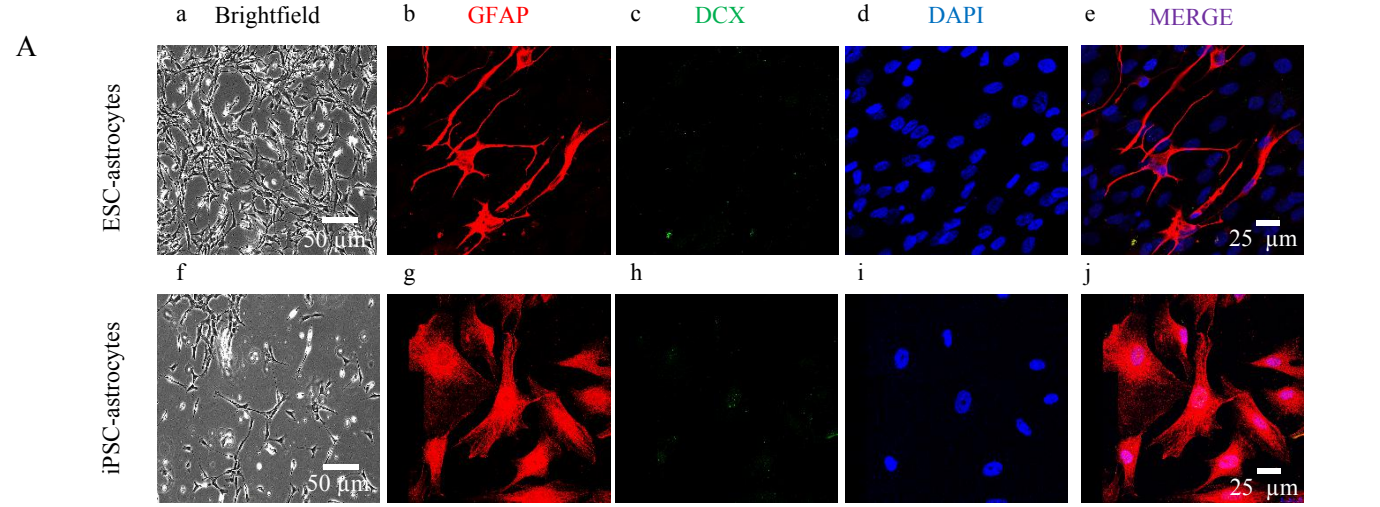
A
a Brightfield
b GFAP
c DCX
d DAPI
e MERGE
ESC-astrocytes
iPSC-astrocytes
50 µm
25 µm
f
g
h
i
j

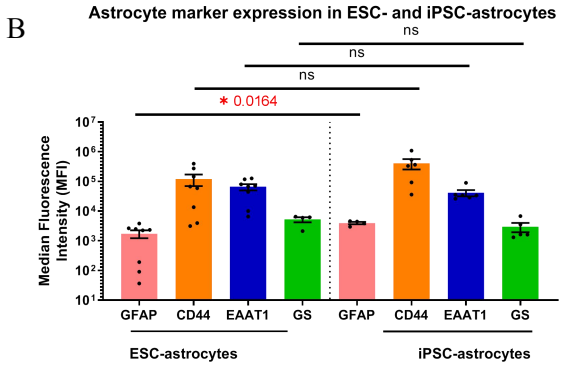
B
Astrocyte marker expression in ESC- and iPSC-astrocytes
Median Fluorescence Intensity (MFI)
ns
ns
ns
* 0.0164
GFAP
CD44
EAAT1
GS
ESC-astrocytes
iPSC-astrocytes

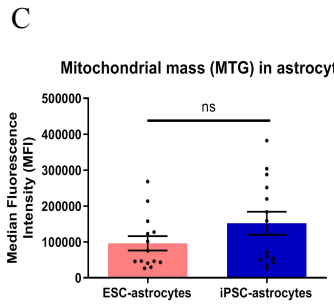
C
Mitochondrial mass (MTG) in astrocytes
Median Fluorescence Intensity (MFI)
ns
ESC-astrocytes
iPSC-astrocytes

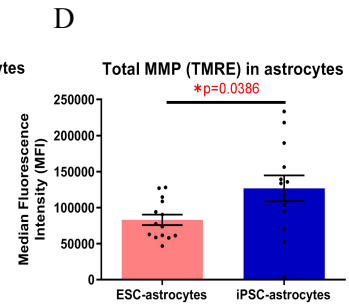
D
Total MMP (TMRE) in astrocytes
Median Fluorescence Intensity (MFI)
*p=0.0386
ESC-astrocytes
iPSC-astrocytes

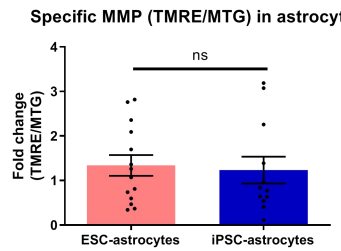
E
Specific MMP (TMRE/MTG) in astrocytes
Fold change (TMRE/MTG)
ns
ESC-astrocytes
iPSC-astrocytes

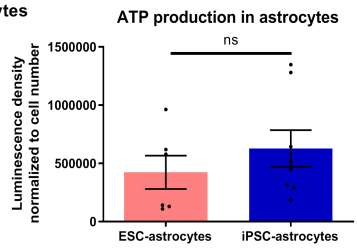
F
ATP production in astrocytes
Luminescence density normalized to cell number
ns
ESC-astrocytes
iPSC-astrocytes

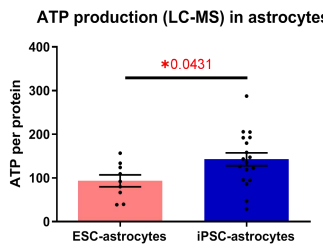
G
ATP production (LC-MS) in astrocytes
ATP per protein
*0.0431
ESC-astrocytes
iPSC-astrocytes

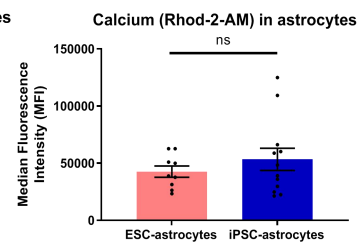
H
Calcium (Rhod-2-AM) in astrocytes
Median Fluorescence Intensity (MFI)
ns
ESC-astrocytes
iPSC-astrocytes

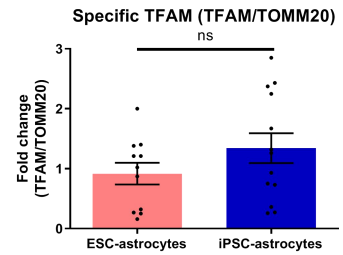
I
Specific TFAM (TFAM/TOMM20)
Fold change (TFAM/TOMM20)
ns
ESC-astrocytes
iPSC-astrocytes

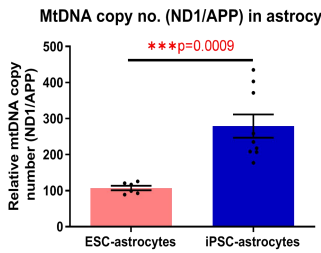
J
MtDNA copy no. (ND1/APP) in astrocytes
Relative mtDNA copy number (ND1/APP)
***p=0.0009
ESC-astrocytes
iPSC-astrocytes

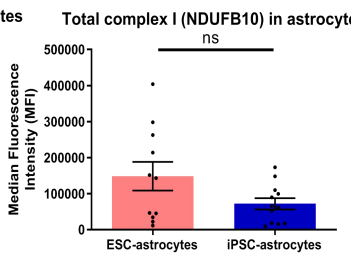
K
Total complex I (NDUFB10) in astrocytes
Median Fluorescence Intensity (MFI)
ns
ESC-astrocytes
iPSC-astrocytes

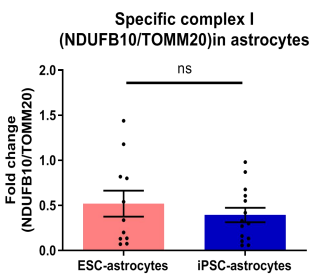
L
Specific complex I (NDUFB10/TOMM20)in astrocytes
Fold change (NDUFB10/TOMM20)
ns
ESC-astrocytes
iPSC-astrocytes

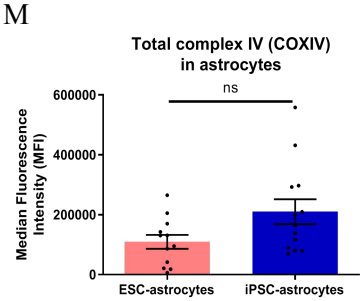
M
Total complex IV (COXIV) in astrocytes
Median Fluorescence Intensity (MFI)
ns
ESC-astrocytes
iPSC-astrocytes

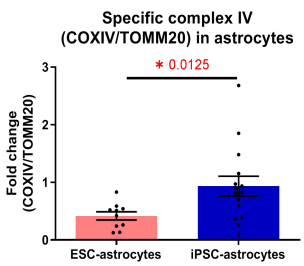
N
Specific complex IV (COXIV/TOMM20) in astrocytes
Fold change (COXIV/TOMM20)
* 0.0125
ESC-astrocytes
iPSC-astrocytes

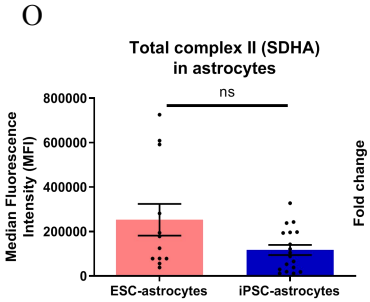
O
Total complex II (SDHA) in astrocytes
Median Fluorescence Intensity (MFI)
ns
ESC-astrocytes
iPSC-astrocytes

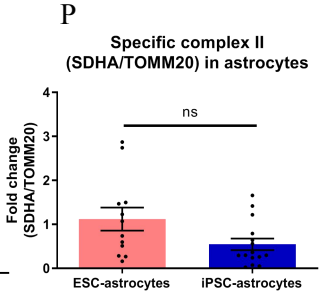
P
Specific complex II (SDHA/TOMM20) in astrocytes
Fold change (SDHA/TOMM20)
ns
ESC-astrocytes
iPSC-astrocytes

Figure 4

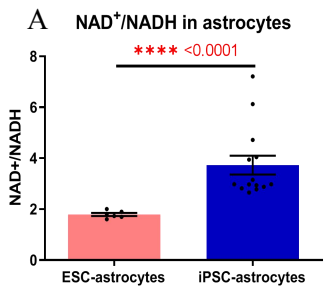
A
NAD+/NADH in astrocytes
**** <0.0001
NAD+/NADH
ESC-astrocytes
iPSC-astrocytes

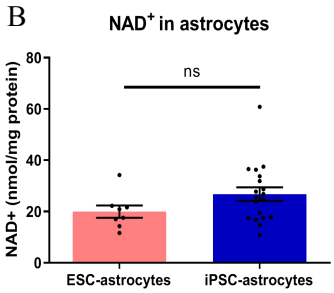
B
NAD+ in astrocytes
ns
NAD+ (nmol/mg protein)
ESC-astrocytes
iPSC-astrocytes

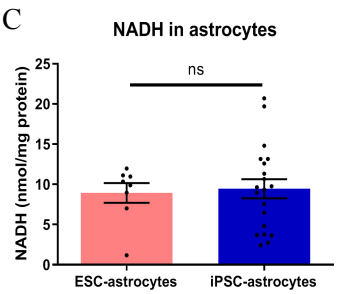
C
NADH in astrocytes
ns
NADH (nmol/mg protein)
ESC-astrocytes
iPSC-astrocytes

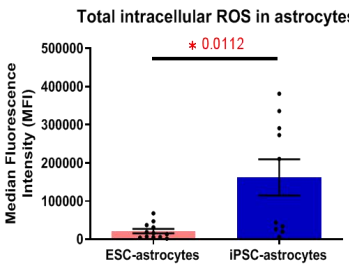
D
Total intracellular ROS in astrocytes
* 0.0112
Median Fluorescence Intensity (MFI)
ESC-astrocytes
iPSC-astrocytes

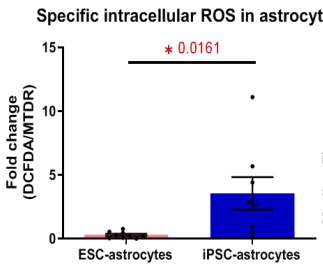
E
Specific intracellular ROS in astrocytes
* 0.0161
Fold change (DCFDA/MTDR)
ESC-astrocytes
iPSC-astrocytes

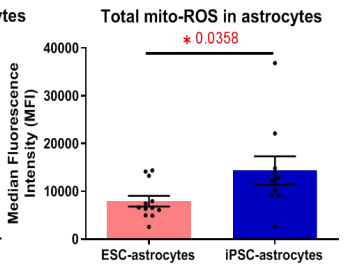
F
Total mito-ROS in astrocytes
* 0.0358
Median Fluorescence Intensity (MFI)
ESC-astrocytes
iPSC-astrocytes

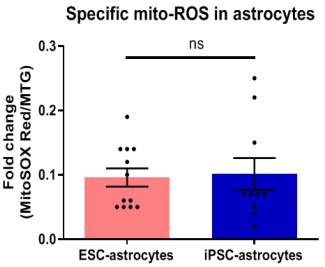
G
Specific mito-ROS in astrocytes
ns
Fold change (MitoSOX Red/MTG)
ESC-astrocytes
iPSC-astrocytes

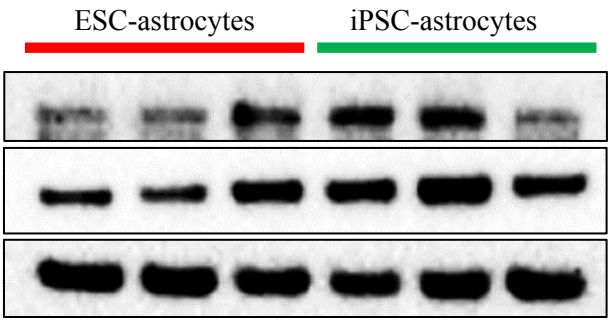
H
ESC-astrocytes
iPSC-astrocytes
PGC-1α
~91kDa
p-SIRT1
(Ser47)
~120 kDa
GAPDH
~37 kDa

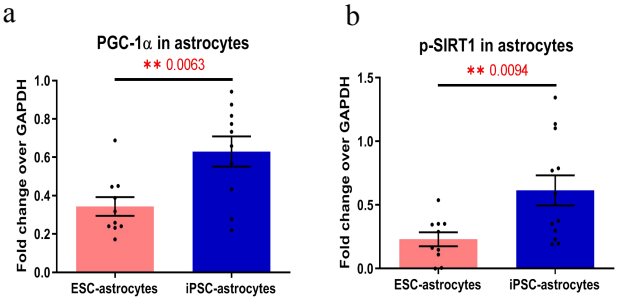
I
a
PGC-1α in astrocytes
** 0.0063
Fold change over GAPDH
ESC-astrocytes
iPSC-astrocytes
b
p-SIRT1 in astrocytes
** 0.0094
Fold change over GAPDH
ESC-astrocytes
iPSC-astrocytes

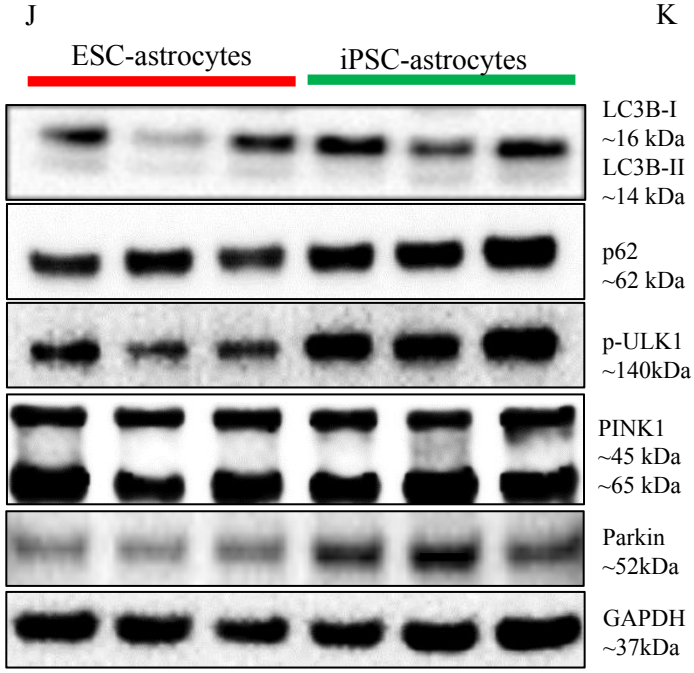
J
ESC-astrocytes
iPSC-astrocytes
LC3B-I
~16 kDa
LC3B-II
~14 kDa
p62
~62 kDa
p-ULK1
~140kDa
PINK1
~45 kDa
~65 kDa
Parkin
~52kDa
GAPDH
~37kDa

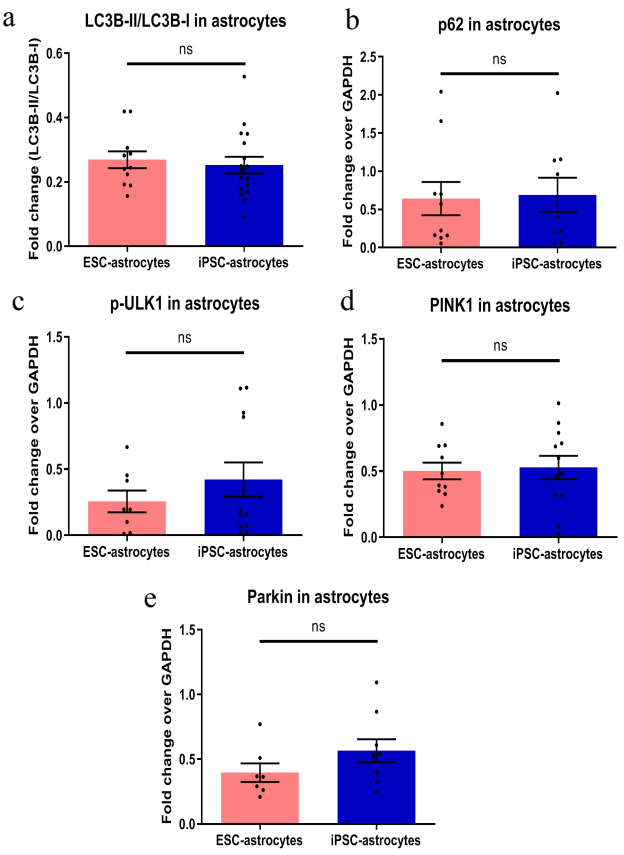
K
a
LC3B-II/LC3B-I in astrocytes
ns
Fold change (LC3B-II/LC3B-I)
ESC-astrocytes
iPSC-astrocytes
b
p62 in astrocytes
ns
Fold change over GAPDH
ESC-astrocytes
iPSC-astrocytes
c
p-ULK1 in astrocytes
ns
Fold change over GAPDH
ESC-astrocytes
iPSC-astrocytes
d
PINK1 in astrocytes
ns
Fold change over GAPDH
ESC-astrocytes
iPSC-astrocytes
e
Parkin in astrocytes
ns
Fold change over GAPDH
ESC-astrocytes
iPSC-astrocytes